

Converting the signal-recycling cavity into an unstable optomechanical filter to enhance the detection bandwidth of gravitational-wave detectors

Joe Bentley, Philip Jones, Denis Martynov, Andreas Freise, and Haixing Miao
*Institute for Gravitational Wave Astronomy, School of Physics and Astronomy,
University of Birmingham, Birmingham B15 2TT, United Kingdom*

(Dated: May 27, 2022)

Current and future interferometric gravitational-wave detectors are limited predominantly by shot noise at high frequencies. Shot noise is reduced by introducing arm cavities and signal recycling, however, there exists a trade-off between the peak sensitivity and bandwidth. This comes from the accumulated phase of signal sidebands when propagating inside the arm cavities. One idea is to cancel such a phase by introducing an unstable optomechanical filter. The original design proposed in [Phys. Rev. Lett. **115**, 211104 (2015)] requires an additional optomechanical filter coupled externally to the main interferometer. Here we consider a simplified design that converts the signal-recycling cavity itself into the unstable filter by using one mirror as a high-frequency mechanical oscillator and introducing an additional pump laser. However, the enhancement in bandwidth of this new design is less than the original design given the same set of optical parameters. The peak sensitivity improvement factor depends on the arm length, the signal-recycling cavity length, and the final detector bandwidth. For a 4 km interferometer, if the final detector bandwidth is around 2 kHz, with a 20 m signal-recycling cavity, the shot noise can be reduced by 10 decibels, in addition to the improvement introduced by squeezed light injection. We also find that the thermal noise of the mechanical oscillator is amplified at low frequencies relative to the vacuum noise, while having a flat spectrum at high frequencies.

I. INTRODUCTION

Recent detections of binary black hole (BBH) and binary neutron star (BNS) mergers [1–3] (catalogued in [4]) have prompted significant research into how the broadband and high-frequency sensitivity of gravitational wave detectors can be increased. Improving the broadband sensitivity would increase the signal-to-noise ratio (SNR) of currently visible events, while decreasing the high-frequency shot noise will allow the determination of the neutron star equation of state [5, 6].

Current ground-based gravitational-wave (GW) detectors such as Advanced LIGO [7] and VIRGO [8], as well as future proposed detectors such as Cosmic Explorer [9] and Einstein Telescope [10] are all limited by the quantum shot noise at high frequencies. This is a fundamental noise source that arises due to the intrinsic quantum uncertainty in the number of individual photons arriving at the photodetector. Arm cavities are used to repeatedly reflect the light in the arm cavities, effectively increasing the path length travelled by the light and amplifying the effect of the GW strain on its phase. The arm cavities also resonantly enhance the carrier and increase the intracavity intensity, thereby reducing the relative photon number uncertainty and thus the shot noise. However, there exists a strict trade-off between the peak sensitivity and detection bandwidth called the *Mizuno limit* or *peak sensitivity-bandwidth product* [11] which applies in general to quantum position measurement devices using a resonant cavity [12–14]. This arises due to the positive dispersion of the arm cavities: when the sideband frequency is near zero the light is resonantly enhanced by constructive interference, however as the sideband frequency is increased the light begins to destructively interfere. The trade-off is also related to the finite storage of energy within the arm cavities [14]. One approach to improving the quantum-limited sensitivity is a direct reduction of the quantum fluctuations using squeezed light injection

[15–21], or internal squeezing [22–25]. Squeezed light injection will be included in future upgrades to Advanced LIGO [26–28], as well as in Cosmic Explorer [9] and Einstein Telescope [29], and has been demonstrated experimentally in GEO600 and LIGO [30, 31], and as a long-term application in GEO600 [32]. However, in light of the Mizuno limit, we will take another approach, instead broadening the bandwidth of the detector by introducing a medium with negative dispersion to compensate for the phase gained in the arm cavity, creating a so-called white light cavity [33–36]. Previously, atomic systems have been used to classically demonstrate bandwidth broadening via negative dispersion [37–40]. Another approach is to use optomechanical coupling such as the unstable optomechanical filter [41] as well as more recent work using optomechanical resonators [42]. After the bandwidth is broadened, the Mizuno limit can be used to increase the peak sensitivity by decreasing the broadened bandwidth.

Previous detector designs including an unstable optomechanical filter (namely [41, 43]) have considered so-called “reflection-readout” based designs. In these designs, the unstable filter is externally coupled to the main interferometer as shown in Fig. 1 (a), requiring drastic alterations of the detector topology. In this paper, we instead propose a simpler “transmission-readout” based design shown in Fig. 1 (b), instead requiring only the conversion of a steering mirror into a high-frequency mechanical oscillator in the signal recycling cavity, and the presence of a pump laser at $\omega_0 + \omega_m$. As an example we apply the design to an example 4km interferometer whose parameters are described in Fig. 2, showing that for a detector bandwidth of 1.8 kHz the shot noise can be reduced by 10 decibels as shown in Fig. 2 (b), however the bandwidth improvement is limited compared to reflection-readout designs as discussed toward the end of Sec. III. The enhancement factor over a tuned Michelson as a function of final detector bandwidth is shown in Fig. 2 (a).

The outline of this paper is as follows. In Sec. II we will

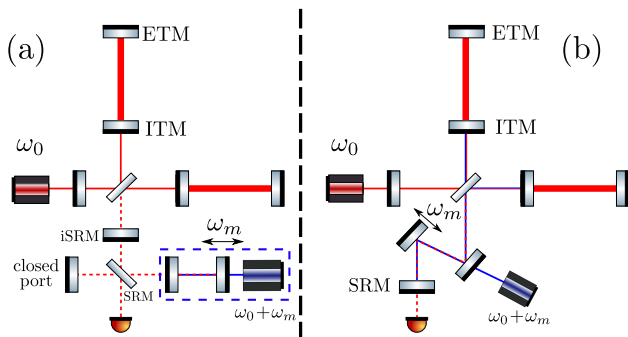


FIG. 1. Figure (a) shows a reflection-readout design such as in [43]. The unstable filter alone is highlighted by the blue dashed box. Figure (b) shows the new transmission-readout setup proposed in this paper. The signal recycling cavity is pumped with laser light at $\omega_0 + \omega_m$, and the mirror above the signal recycling mirror is mechanically suspended with mechanical resonance frequency ω_m . ETM: End Test Mass, ITM: Input Test Mass, SRM: Signal Recycling Mirror, iSRM: Internal SRM (to form an impedance-matched cavity with the ITM)

give a brief overview of the unstable filter originally presented in [41], including its setup and what properties we require of it. In Sec. III we will discuss the new transmission-readout setup, deriving the quantum noise spectral density as well as the noise contribution from the thermal noise of the mechanical oscillator. We will then compare the peak sensitivity improvement achieved over a tuned signal-recycled Michelson interferometer as shown in Fig. 2, and discuss the thermal noise of the mechanical oscillator shown in Fig. 5. Finally in Sec. IV we will discuss how our results compare to previous reflection-readout setups, the thermal noise and how it can be mitigated with optical dilution, as well as future developments involving the transmission-readout setup.

II. OVERVIEW OF UNSTABLE FILTER

In this section the motivation and concept of negative dispersion will be given, followed by a brief overview of the unstable filter as a specific realization of this concept. For more details on the unstable filter itself refer to [41].

In a standard tuned Michelson interferometer the arm cavities are tuned to the carrier light frequency ω_0 so that $2\omega_0 L_{\text{arm}}/c = 2\pi N$ where N is an integer, L_{arm} is the arm cavity length, and ω_0 is the laser carrier frequency. A GW will induce a change in path length between the ITM and ETM oppositely for both arms, modulating the carrier light to induce signal sidebands at $\omega_0 \pm \Omega$, with Ω being the GW frequency. Since the arm cavities are tuned to the carrier light these signal sidebands will not be completely resonant in the arm cavities, as they obtain an extra round-trip phase of $2\Omega L_{\text{arm}}/c$ away from the perfect resonant condition which will therefore accrue destructively. As the GW frequency Ω increases, as does this extra round-trip phase, leading to more destructive interference and further reducing the signal strength. Therefore the arm cavities lead to decreasing sensitivity at higher frequen-

cies. We therefore envisage a negative dispersion device that gives a round-trip phase exactly cancelling that gained in a round-trip through the arm cavity, so that the round-trip phase gained through this device is $-2\Omega L_{\text{arm}}/c$. This will cancel the attenuation of the signal due to positive dispersion and effectively broaden the bandwidth of the detector.

The unstable filter, highlighted in Fig. 1, is just one such realization of a negative dispersion device. It is an optomechanical device consisting of a cavity with resonant frequency ω_0 with a fixed input mirror and a movable end mirror as a mechanical oscillator with mechanical resonant frequency ω_m and quality factor Q_m ; the entire cavity pumped by laser light at frequency $\omega_0 + \omega_m$. Signal sidebands at frequency $\omega_0 \pm \Omega$ enter the unstable filter and beat with the pump field at $\omega_0 + \omega_m$, producing a radiation pressure force fluctuating at frequency $\omega_m \pm \Omega$ at the mechanically suspended mirror. This force moves the mirror which modulates the cavity field to further modify the sidebands at $\omega_0 \pm \Omega$, and also modify the mirror's mechanical motion at frequency ω_m . This process is analogous to difference frequency generation, also known as optical parametric amplification, in non-linear optics, see for example p. 9 of [44]. It can be shown that assuming the so-called resolved sideband regime, where the GW sideband frequency $\Omega \ll \gamma_f \ll \omega_m$, and γ_f is the bandwidth of the filter cavity, and also assuming the system is in the unstable regime where the mechanical damping rate $\gamma_m \equiv \omega_m/Q_m$ is much less than negative damping rate due to the optomechanical interaction γ_{opt} , the optical transfer function of the filter cavity takes the form,

$$\frac{\Omega + i\gamma_{\text{opt}}}{\Omega - i\gamma_{\text{opt}}} \approx \exp\left(-\frac{2i\Omega}{\gamma_{\text{opt}}}\right), \quad (1)$$

where $\gamma_{\text{opt}} \equiv g^2/\gamma_f$ is the negative optomechanical damping rate with g —the optomechanical coupling strength—as defined later in Eq. (4). In the second approximation we assumed that $\gamma_{\text{opt}} \gg \Omega$, giving a *linear* negative dispersion. Clearly, the condition to exactly cancel the phase gained in the arm cavities is therefore given by, $\gamma_{\text{opt}} = c/L_{\text{arm}}$.

This enhancement is intuitive for the reflection-readout approaches such as in Fig. 1 (a), because the signal is recycled with a negative phase and reinjected into the arm cavity to cancel the positive phase gained. However this is less intuitive in the transmission-readout approach shown in Fig. 1 (b). Regardless, we will show that bandwidth broadening is still achieved.

III. ANALYSIS

In this section we outline the analysis of the transmission-readout setup—a simplified version of which is shown in Fig. 3 by focusing on the differential mode only. In comparison to the reflection-readout setup in Fig. 1 (a) the arm cavity is no longer coupled directly to the dark port. Instead the arm cavity and filter cavity form an effective three-mirror cavity similar to the twin signal-recycling scheme studied in [45, 46], except with one cavity replaced with the optomechanical filter cavity.

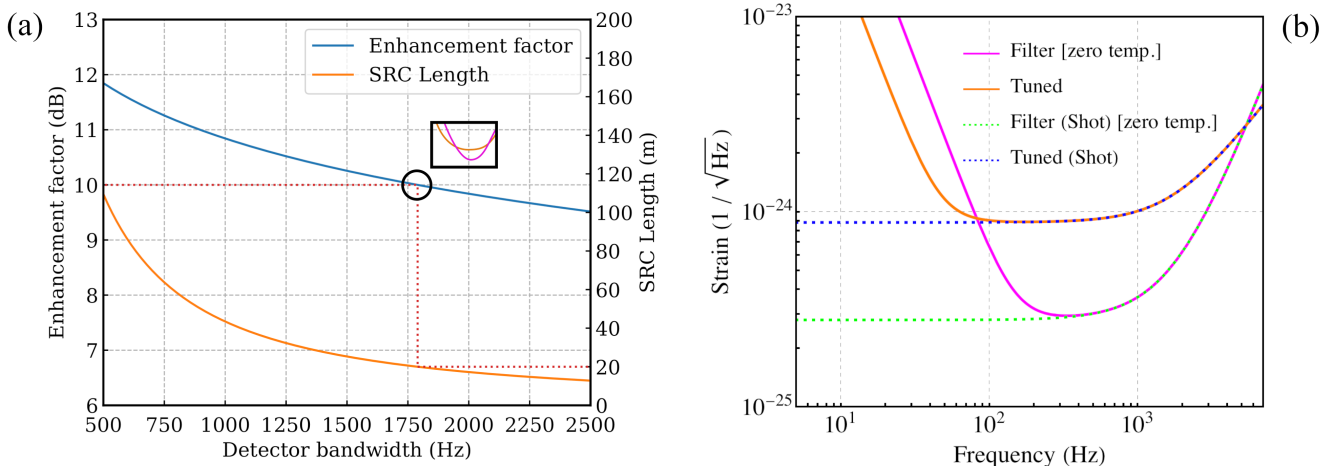


FIG. 2. Figure (a) shows the peak sensitivity improvement ratio of the transmission-readout setup to a tuned signal-recycled Michelson interferometer as a function of broadened detector bandwidth Γ_{detector} as given in Eq. (30). Here advanced LIGO parameters are used (4 km arm length, 40 kg test mass, 800 kW arm power), and additionally an ITM transmissivity of 0.045 and SRM transmissivity of 0.0003 are used. The SRC length solved for the detector bandwidth is also plotted to show how it could be varied to improve the peak sensitivity with these transmissivities. The dotted line is plotted for our chosen SRC length of 20 m, giving a detector bandwidth of around 1790 Hz, and therefore an enhancement factor of 10 dB. The circled value and inset highlights the chosen values used in figure (b), which shows the total quantum noise with the unstable filter mirror at zero temperature. The tuned Michelson bandwidth set to the effective bandwidth of the new transmission readout setup as discussed at the end of Sec. III. We also assume 10 dB frequency-dependent squeezing over the entire frequency range as outlined in [16].

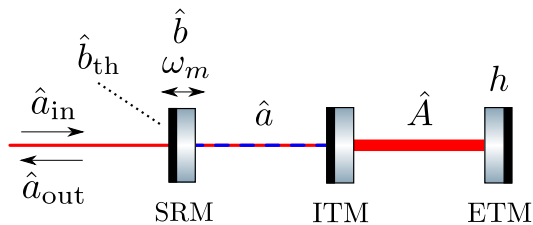


FIG. 3. Figure showing the setup analysed in Sec. III, which is a simplified version of Fig. 1 (b). \hat{a} describes the unstable filter cavity mode, \hat{A} describes the differential arm cavity mode, \hat{b} is the mirror oscillation mode, h is the GW strain signal, and the mirror is coupled to an external heat bath described by the continuum field \hat{b}_{th} , shown by the dotted line. The cavity field \hat{a} is coupled to the external continuum fields $\hat{a}_{\text{in}}, \hat{a}_{\text{out}}$.

To analyse the system we use a Hamiltonian-based approach based on [47–49], which was previously used to analyse the reflection-readout setup in [41]. This approach is valid under the *single-mode approximation* where the GW sideband frequency $\Omega/(2\pi) \ll \text{FSR}$ where FSR is the free spectral range, i.e. only modes within one free spectral range are considered. This can be important for long-baseline facilities such as the 40 km Cosmic Explorer [9] where the free spectral range is only 3.75 kHz.

The approach consists of first writing the Hamiltonian for the system, which, referring again to Fig. 3, consists of SRC mode \hat{a} and differential arm cavity mode \hat{A} , as well as a mechanically suspended mirror which is modelled as a damped-driven harmonic oscillator with resonant frequency ω_m and mechanical damping rate γ_m which is described by mode \hat{b} .

The mirror is additionally coupled to an external continuous mode \hat{b}_{th} which represents an external heat bath. The equations of motion are then computed using Heisenberg’s equation of motion, and they are then solved in the frequency-domain to give an equation for an output field at the dark port \hat{a}_{out} in terms of input fields \hat{a}_{in} and the GW strain h . The two-photon quadratures [16, 50] are then computed, and hence the spectral density for the quadrature operators. The external fields $\hat{a}_{\text{in}}, \hat{a}_{\text{out}}$, and \hat{b}_{th} describe freely propagating continuous mode fields as in [51].

The total Hamiltonian is given by $\hat{H}_{\text{tot}} = \hat{H}_0 + \hat{H}_{\text{int}}^{\text{filter}} + \hat{H}_{\text{int}}^{\text{ETM}} + \hat{H}_{\gamma_f} + \hat{H}_{\gamma_m} + \hat{H}_{\gamma_{\text{arm}}}$. \hat{H}_0 is the free part, $\hat{H}_{\text{int}}^{\text{filter}}$ describes the interaction between the SRC mode and the mechanically suspended mirror, $\hat{H}_{\text{int}}^{\text{ETM}}$ describes the radiation pressure coupling between the ETM and arm cavity field as well as to the GW strain (we choose the ITM to be static without loss of generality), \hat{H}_{γ_f} describes the coupling of the SRC to the external continuous vacuum field (the dark port) as discussed in [47] (see footnote [52] for further discussion on this analysis) and $\gamma_f = T_{\text{SRM}}c/(4L_{\text{SRC}})$ —where T_{SRM} is the SRM power transmissivity and L_{SRC} is the length of the signal recycling cavity—is the coupling constant of the SRC to the external field, \hat{H}_{γ_m} describes the coupling of the mirror to the external heat bath \hat{b}_{th} with coupling constant $\gamma_m = \omega_m/Q_m$ —where ω_m is the mirror eigenfrequency and Q_m is the mechanical quality factor—whose equation of motion will be the quantum Langevin equation [53] [54, p. 158], and finally $\hat{H}_{\gamma_{\text{arm}}}$ describes the coupling between the SRC and the arm cavity [45, 46].

The free Hamiltonian \hat{H}_0 is given by,

$$\hat{H}_0 = \frac{\hat{p}^2}{2m} + \frac{1}{2}m\omega_m^2\hat{x}^2 + \hbar\omega_0\hat{a}^\dagger\hat{a} + \hbar\omega_0\hat{A}^\dagger\hat{A} + \frac{\hat{p}^2}{2M}, \quad (2)$$

where \hat{P} is the ETM momentum, and $M = m_{\text{test}}/4$ is the reduced mass of the differential arm cavity mode \hat{A} , and m_{test} being the actual mirror mass [55, 56]; ω_0 is the carrier frequency of the main interferometer laser and also the resonant frequency of the arm cavities; \hat{p} is the mechanically suspended mirror momentum, \hat{x} is its position, and m is its mass. The filter cavity field \hat{a} is pumped by a laser at frequency $\omega_0 + \omega_m$ resulting in a mean photon number \bar{a} . The linearised filter interaction Hamiltonian is given by [41, 47, 48],

$$\hat{H}_{\text{int}}^{\text{filter}} = -\hbar g_0[\hat{a}e^{i(\omega_0+\omega_m)t} + \hat{a}^\dagger e^{-i(\omega_0+\omega_m)t}]\hat{x}, \quad (3)$$

where $g_0 = \omega_0/L_f\bar{a}$, $\bar{a} = [2P_f L_f/(\hbar\omega_0 c)]^{1/2}$, where P_f is the circulating power in the filter cavity and L_f is the length of the filter cavity. The mirror displacement can be written in the Heisenberg picture as $\hat{x} = x_q(\hat{b}e^{-i\omega_m t} + \hat{b}^\dagger e^{i\omega_m t})$, where x_q is the ground-state harmonic oscillator position uncertainty, $x_q = \sqrt{\hbar/(2m\omega_m)}$. We then move into the rotating frame at ω_0 and disregard the $\omega_0 + 2\omega_m$ sideband by invoking the rotating wave approximation (RWA), since $\gamma_f \ll \omega_m$ for any frequency of interest, however this approximation should be relaxed for a full analysis. The interaction Hamiltonian therefore becomes, [41]

$$\hat{H}_{\text{int}}^{\text{filter}} \approx -\hbar g(\hat{a}\hat{b} + \hat{a}^\dagger\hat{b}^\dagger), \quad (4)$$

where $g = g_0 x_q$.

For the ETM dynamics we have a term due to the effective GW interaction with the mirror, and another due to the linearised radiation pressure interaction between the mirror and arm cavity field,

$$\hat{H}_{\text{int}}^{\text{ETM}} = F_{\text{GW}}\hat{X} - \hbar G_0(\hat{A} + \hat{A}^\dagger)\hat{X}, \quad (5)$$

where $F_{\text{GW}} = ML_{\text{arm}}\ddot{h}$ is the GW tidal force, $G_0 = \omega_0/L_{\text{arm}}\bar{A}$, and $\bar{A} = [2P_{\text{arm}}L_{\text{arm}}/(\hbar\omega_0 c)]^{1/2}$, where P_{arm} is the arm cavity power, L_{arm} is the arm cavity length.

Finally there is sloshing (transfer of excitation) between the SRC and arm cavity [45, 46], which leads to the interaction term,

$$\hat{H}_{\gamma_{\text{arm}}} = i\hbar\omega_S(\hat{a}\hat{A}^\dagger - \hat{a}^\dagger\hat{A}), \quad (6)$$

where $\omega_S \approx \sqrt{c\gamma_{\text{arm}}/L_{\text{SRC}}}$ is called the ‘‘sloshing frequency’’, with L_{SRC} being the length of the signal-recycling cavity, and $\gamma_{\text{arm}} = T_{\text{ITMC}}/(4L_{\text{arm}})$ is the arm cavity bandwidth, with T_{ITMC} being the power transmissivity of the ITM.

Therefore we obtain the full set of equations of motion,

$$\dot{\hat{a}}_{\text{out}} = \hat{a}_{\text{in}} - \sqrt{2\gamma_f}\hat{a} \quad (7)$$

$$\dot{\hat{a}} + \gamma_f\hat{a} = ig\hat{b}^\dagger + \sqrt{2\gamma_f}\hat{a}_{\text{in}} - \omega_S\hat{A} \quad (8)$$

$$\dot{\hat{b}} + \gamma_m\hat{b} = ig\hat{a}^\dagger + \sqrt{2\gamma_m}\hat{b}_{\text{th}} \quad (9)$$

$$\dot{\hat{A}} = \omega_S\hat{a} + iG_0\hat{X} \quad (10)$$

$$\dot{\hat{X}} = \hat{P}/M \quad (11)$$

$$\dot{\hat{P}} = -ML\ddot{h} + \hbar G_0(\hat{A} + \hat{A}^\dagger), \quad (12)$$

where γ_f is the filter cavity bandwidth as defined above.

These equations are then transformed to the frequency domain, noting that the property of the Fourier transform $\mathcal{F}[\hat{a}^\dagger(t)] = (\hat{a}^\dagger)(-\Omega)$ which we will simply denote as $\hat{a}^\dagger(-\Omega)$. The equations are then solved to calculate the output field $\hat{a}_{\text{out}}(\Omega)$ in terms of the input fields $\hat{a}_{\text{in}}(\Omega)$, $\hat{a}_{\text{in}}^\dagger(-\Omega)$ and the GW strain signal $h(\Omega)$. Note that since $h(t)$ is real, $h(\Omega) = h^*(-\Omega)$. From these transfer functions a sideband input-output relation can be constructed of the form,

$$\begin{bmatrix} \hat{a}_{\text{out}}(\Omega) \\ \hat{a}_{\text{out}}^\dagger(-\Omega) \end{bmatrix} \equiv \mathbb{M}_s \begin{bmatrix} \hat{a}_{\text{in}}(\Omega) \\ \hat{a}_{\text{in}}^\dagger(-\Omega) \end{bmatrix} + \mathbb{M}_s^{\text{th}} \begin{bmatrix} \hat{b}_{\text{th}}(\Omega) \\ \hat{b}_{\text{th}}^\dagger(-\Omega) \end{bmatrix} + \vec{D}_s h(\Omega), \quad (13)$$

where \mathbb{M}_s is the transfer matrix of the input field to the output field at the dark port for the single-photon (sideband) modes, representing the overall linearised dynamics of the system, similarly \mathbb{M}_s^{th} is the transfer matrix for the thermal noise to the dark port output field, and \vec{D}_s represents the linearised coupling of the GW strain signal into the upper and lower sidebands of the dark port output field.

There is another independent contribution to the noise: the thermal noise arising from the coupling of the mechanically suspended mirror to the fluctuating environmental heat bath \hat{b}_{th} at temperature T . The heat bath provides random thermal fluctuations whose statistics are determined by the Bose-Einstein distribution, which for $k_B T \gg \hbar\omega_m$ leads to a spectral density given approximately by [41, 48],

$$S_{\hat{b}_{\text{th}}}(\Omega) = \frac{2k_B T}{\hbar\omega_m} + 1. \quad (14)$$

To calculate the power spectral density (PSD) due to the quantum noise we use the two-photon formalism using quadrature operators \hat{O}_1, \hat{O}_2 —respectively called the amplitude and phase quadratures—with the input quadratures at the dark port having a flat spectral density equal to unity. These quadrature operators are related to the single-photon (sideband) operators by a unitary transformation,

$$\begin{bmatrix} \hat{O}_1 \\ \hat{O}_2 \end{bmatrix} = \frac{1}{\sqrt{2}} \begin{bmatrix} 1 & 1 \\ -i & i \end{bmatrix} \begin{bmatrix} \hat{O}(\Omega) \\ \hat{O}^\dagger(-\Omega) \end{bmatrix} \equiv \mathbb{U} \begin{bmatrix} \hat{O}(\Omega) \\ \hat{O}^\dagger(-\Omega) \end{bmatrix}. \quad (15)$$

We need to compute the transfer functions between the output quadratures and the input quadratures and strain signal of the form,

$$\begin{bmatrix} \hat{a}_1^{\text{out}} \\ \hat{a}_2^{\text{out}} \end{bmatrix} = \mathbb{M}_q \begin{bmatrix} \hat{a}_1^{\text{in}} \\ \hat{a}_2^{\text{in}} \end{bmatrix} + \mathbb{M}_q^{\text{th}} \begin{bmatrix} \hat{b}_1^{\text{th}} \\ \hat{b}_2^{\text{th}} \end{bmatrix} + \vec{D}_q h(\Omega), \quad (16)$$

where $\hat{a}_{1,2}^{\text{in}}$ and $\hat{a}_{1,2}^{\text{out}}$ are the quadratures at the optical input and output port respectively, and $\hat{b}_{1,2}^{\text{th}}$ are the quadratures input from the thermal heat bath. The relation between the quadrature transfer matrices and the sideband transfer matrices in Eq. (13) are given by,

$$\mathbb{M}_q = \mathbb{U}\mathbb{M}_s\mathbb{U}^\dagger, \quad \mathbb{M}_q^{\text{th}} = \mathbb{U}\mathbb{M}_s^{\text{th}}\mathbb{U}^\dagger, \quad \vec{D}_q = \mathbb{U}\vec{D}_s. \quad (17)$$

The output quadrature operator for a homodyne measurement of homodyne angle ζ is given by $\hat{a}_\zeta^{\text{out}} = (\hat{a}_1^{\text{out}}, \hat{a}_2^{\text{out}})$.

$(\cos \zeta, \sin \zeta)^T$. To calculate the spectral density we first separate the output quadrature into a zero-mean noise term and a mean signal term, $\hat{a}_\zeta^{\text{out}} = \Delta \hat{a}_\zeta^{\text{out}} + \langle \hat{a}_\zeta^{\text{out}} \rangle$, where,

$$\Delta \hat{a}_\zeta^{\text{out}} = \left(\left[\mathbb{M}_q \left(\hat{a}_1^{\text{in}} \right) \right]^T + \left[\mathbb{M}_q^{\text{th}} \left(\hat{b}_1^{\text{th}} \right) \right]^T \right) \cdot \begin{pmatrix} \cos \zeta \\ \sin \zeta \end{pmatrix}, \quad (18)$$

$$|\langle \hat{a}_\zeta^{\text{out}} \rangle|^2 = |\vec{D}_q^{(1)} \cos \zeta + \vec{D}_q^{(2)} \sin \zeta|^2 / |h|^2 \quad (19)$$

where $\vec{D}_q^{(i)}$ is the i -th element of \vec{D}_q .

The single-sided PSD $S_{OO}(\Omega)$ of an operator $\hat{O}(\Omega)$ for an input vacuum state $|0\rangle$ is given by the symmetrised covariance, $\langle 0 | \hat{O}(\Omega) \hat{O}^\dagger(\Omega') | 0 \rangle_{\text{sym}} = \pi S_{OO}(\Omega) \delta(\Omega - \Omega')$ [16, 57, 58]. First calculating the vacuum noise for $\hat{a}_\zeta^{\text{out}}$, using that $\langle 0 | \hat{a}_i^{\text{in}}(\Omega) \hat{a}_j^{\text{in}\dagger}(\Omega') | 0 \rangle_{\text{sym}} = \pi \delta_{ij} \delta(\Omega - \Omega')$, and then dividing by the strain transfer function, we find the PSD of the vacuum noise superimposed on the strain measurement is,

$$S_h^\zeta(\Omega) = \frac{(\cos \zeta, \sin \zeta) \mathbb{M}_q(\Omega) \mathbb{M}_q^T(\Omega) (\cos \zeta, \sin \zeta)^T}{|\vec{D}_q^{(1)} \cos \zeta + \vec{D}_q^{(2)} \sin \zeta|^2}. \quad (20)$$

Assuming that $\gamma_m \ll \Omega$, we find that the strain-referred shot-noise limited PSD is given by,

$$S_h^{\text{shot}}(\Omega) = \frac{\Omega^2 \gamma_f^2 + (g^2 - \omega_S^2 + \Omega^2)^2}{4G_0^2 L_{\text{arm}}^2 \gamma_f \omega_S^2} + \frac{g^2 \gamma_m \left(\frac{2k_B T}{\hbar \omega_m} + 1 \right)}{G_0^2 L_{\text{arm}}^2 \omega_S^2}, \quad (22)$$

and the radiation-pressure limited PSD is given by,

$$S_h^{\text{rp}}(\Omega) = \frac{4G_0^2 \hbar^2 \omega_S^2}{M^2 \Omega^4 L_{\text{arm}}^2 \left[\Omega^2 \gamma_f^2 + (g^2 - \omega_S^2 + \Omega^2)^2 \right]} \left[\gamma_f + \frac{g^2 \gamma_m}{\Omega^2} \left(\frac{2k_B T}{\hbar \omega_m} + 1 \right) \right], \quad (23)$$

where in both cases the former term is the vacuum contribution and the latter term $\propto \gamma_m$ is the thermal contribution.

The total strain-referred vacuum-limited PSD can be written in the form,

$$S_{\text{vacuum}}(\Omega) \equiv S_h(\Omega)|_{T=0} = \left(\frac{1}{\mathcal{K}} + \mathcal{K} \right) \frac{h_{\text{SQL}}^2}{2} \geq h_{\text{SQL}}^2. \quad (24)$$

Here $h_{\text{SQL}}^2 \equiv 2\hbar/(M\Omega^2 L_{\text{arm}}^2) = 8\hbar/(m_{\text{test}}\Omega^2 L_{\text{arm}}^2)$ is the *standard quantum limit* [16, 57, 59], and \mathcal{K} is a dimensionless factor given by,

$$\mathcal{K} \equiv \frac{8P_{\text{arm}}\omega_0}{ML_{\text{arm}}c} \frac{\gamma_f \omega_S^2}{\Omega^2 (\Omega^2 \gamma_f^2 + (g^2 + \Omega^2 - \omega_S^2)^2)}, \quad (25)$$

where the radiation pressure coupling constant G_0 has been written out fully.

The transmission-readout shot noise spectral density (given by Eq. (22)) matches peak sensitivity (shot noise PSD at $\Omega = 0$) of a tuned signal-recycled Michelson interferometer if we have the condition,

$$g^2 = \omega_S^2 + \gamma_f \omega_S, \quad (26)$$

and we set the tuned signal-recycled Michelson detector bandwidth $\gamma_{\text{detector}} = \gamma_f$. In this case the peak sensitivity for both

We will assume an ideal phase quadrature measurement ($\zeta = \pi/2$) at the photodiode, in which case we are only concerned about the output phase quadrature \hat{a}_2^{out} . In this case we have,

$$S_h(\Omega) = \frac{|\mathbb{M}_q^{(2,1)}(\Omega)|^2 + |\mathbb{M}_q^{(2,2)}(\Omega)|^2}{|\vec{D}_q^{(2)}|^2} \equiv S_{\text{vacuum}}^{\text{rp}}(\Omega) + S_{\text{vacuum}}^{\text{shot}}(\Omega). \quad (21)$$

We can follow the same process as above to find the thermal noise fluctuations arising from thermal noise quadrature operators $\hat{b}_{1,2}^{\text{th}}$, noting that the spectral density for the heat bath is given by Eq. (14).

For both the vacuum and thermal noise we define the shot-noise contributions $S_{\text{vacuum}}^{\text{shot}}(\Omega)$ and $S_{\text{thermal}}^{\text{shot}}(\Omega)$ as the spectral density contribution remaining when the mass $M \rightarrow \infty$, and the radiation-pressure contributions $S_{\text{vacuum}}^{\text{rp}}(\Omega)$ and $S_{\text{thermal}}^{\text{rp}}(\Omega)$ as the term remaining when the shot-noise contribution is subtracted from the total spectrum.

the transmission readout setup and tuned Michelson is given by,

$$S_{\text{trans}}^{\text{shot}}(\Omega = 0) = S_{\text{tuned}}^{\text{shot}}(\Omega = 0) = \frac{\gamma_f}{4G_0^2 L_{\text{arm}}^2}. \quad (27)$$

The broadened effective detector bandwidth of the transmission readout setup can be shown to be on the order of $\sqrt{\gamma_f \omega_S}$, or in terms of optical parameters,

$$\Gamma_{\text{detector}} \sim \frac{c}{2\sqrt{2}} \left[\frac{T_{\text{ITM}} T_{\text{SRM}}^2}{L_{\text{arm}} L_{\text{SRC}}^3} \right]^{1/4}. \quad (28)$$

To compare the shot noise limited sensitivity of our setup to a tuned signal-recycled Michelson interferometer, we set the tuned Michelson detector bandwidth to be equal to the effective bandwidth of the transmission readout setup, i.e. $\gamma_{\text{detector}} = \Gamma_{\text{detector}} (= \sqrt{\gamma_f \omega_S})$. In this case the improvement ratio of the peak power spectral densities, i.e. the power ratio of the tuned Michelson to transmission readout setup shot noise power spectral densities at low frequencies,

is given by,

$$\eta \equiv \frac{S_{\text{tuned}}^{\text{shot}}(\Omega = 0)}{S_{\text{trans}}^{\text{shot}}(\Omega = 0)} = \frac{\sqrt{\gamma_f \omega_S}}{\gamma_f} = \sqrt{\frac{\omega_S}{\gamma_f}} \quad (29)$$

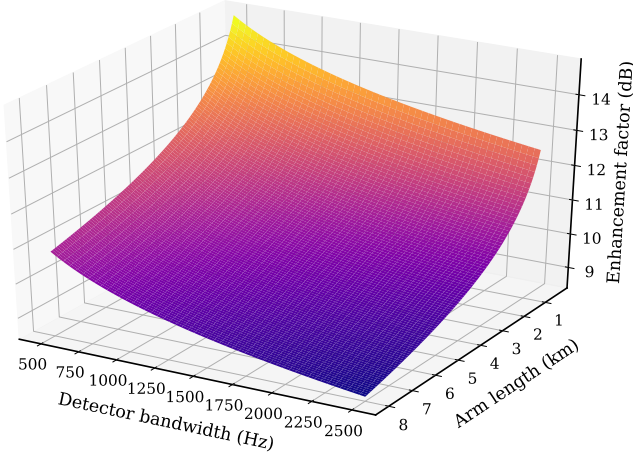


FIG. 4. Surface plot showing the peak sensitivity improvement power ratio of the transmission-readout setup to a tuned Michelson as a function of both detector bandwidth Γ_{detector} and arm length, showing the (log) inverse cube-root dependence of the enhancement factor on the arm length. The parameters are as in Fig. 2.

By solving Eq. (28) for the SRC length, the above improvement factor can be written in terms of the effective bandwidth, arm length, and SRM and ITM power transmissivities as,

$$\eta = \left(\frac{c T_{\text{ITM}}}{\Gamma_{\text{detector}} L_{\text{arm}} T_{\text{SRM}}} \right)^{1/3}. \quad (30)$$

This quantity is shown for various detector bandwidths in Fig. 2 (a), and a surface plot for various arm lengths is shown in Fig. 4. Note that it is proportional to $(T_{\text{ITM}}/T_{\text{SRM}})^{1/3}$, however if the ITM transmissivity T_{ITM} is increased then the arm cavity intracavity power will be decreased and hence the shot noise increased, thereby requiring a higher input power. Similarly if the SRM transmissivity T_{SRM} is very small then losses start to dominate. Finally, note that the enhancement factor for a given effective detector bandwidth decreases as the inverse cube root of the arm cavity length L_{arm} .

For both the shot noise and radiation pressure it was found that the ratio of the absolute value squared of the thermal fluctuation to the vacuum fluctuation noise has the form of a “low-pass filter”. For the shot noise ratio we assume the resolved sideband regime, whereas for the radiation pressure ratio no approximation is made. For the shot noise the effective cutoff frequency is $(g^2 - \omega_S^2)/\gamma_f$. Note that when the replacement $g^2 = \omega_S^2 + \gamma_f \omega_S$ is performed, as described later, the cutoff frequency becomes ω_S . Therefore the thermal noise is suppressed relative to the vacuum noise at high frequencies where shot noise dominates, however for $\gamma_m \ll \Omega$ we find that the contribution is approximately flat as shown in Eq. (22). For the radiation pressure term, the cutoff frequency γ_m is very

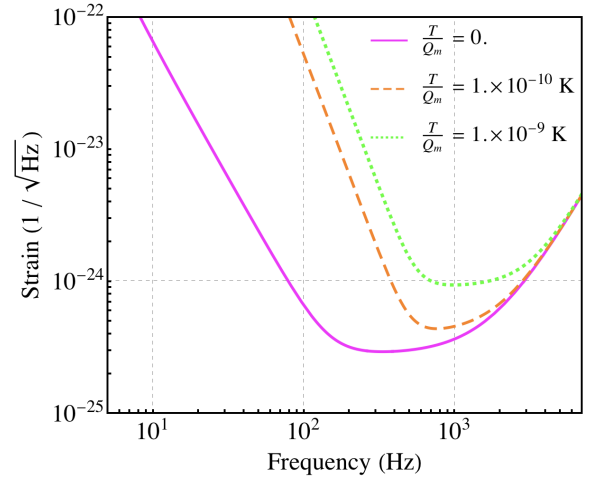


FIG. 5. Figure showing the total quantum noise of the transmission-readout setup after including the thermal noise at various environmental temperatures, using the parameters in Fig. 2, including the detector bandwidth marked by the green star. At low frequencies the thermal noise is amplified relative to the vacuum noise, while at high frequencies it has a flat spectrum.

small compared to Ω , however the gain $g^2/(\gamma_f \gamma_m) \equiv \gamma_{\text{opt}}/\gamma_m$ is very large, and so at low frequencies the thermal noise is much greater than the vacuum noise. Intuitively, at low frequencies the thermal heat bath fluctuations are amplified by the response function of the mechanically suspended mirror in the filter cavity. The total quantum noise plot is shown in Fig. 5. Note that for $\gamma_m \ll \Omega$ the high-frequency thermal noise contribution is balanced by the diminishing strain response and has a flat spectrum as shown in Eq. (22).

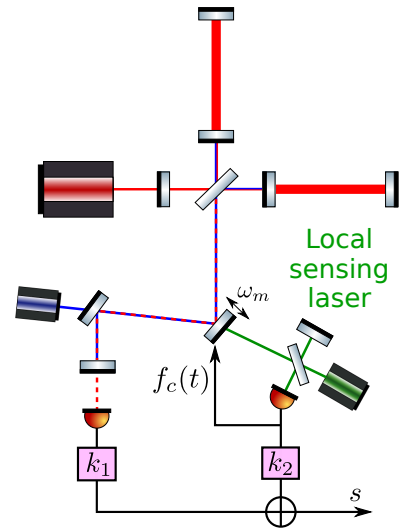


FIG. 6. Figure showing an example of the local sensing control scheme applied to the transmission-readout setup. A control force $f_c(t)$ is applied to the mechanically suspended mirror, whose displacement is read out by the local sensing laser. The local sensing readout and main readout are optimally combined by coefficients k_1 and k_2 to recover the bandwidth broadened sensitivity.

IV. DISCUSSION

As shown above, the amplitude improvement goes as the square root of the effective bandwidth, while the decrease in peak sensitivity of the transmission readout setup goes as the effective bandwidth, and therefore we are limited in the improvement we can achieve before we start to degrade the overall sensitivity. For the previous reflection-readout setups, the effective bandwidth is given by $(\gamma_f \omega_{S_{\text{refl}}})^{1/3}$ (where the sloshing frequency $\omega_{S_{\text{refl}}} = \sqrt{c\gamma_f/L_{\text{arm}}}$ is defined differently from in our analysis since we are measuring in reflection of the unstable filter cavity rather than in transmission [41]), however in that case it can be increased further by decreasing the filter cavity length or increasing the ETM transmissivity without adversely affecting the shot noise or radiation pressure noise.

There is also strong coupling of the thermal noise into the unstable filter, putting a strict requirement on the environmental temperature. This can be mitigated using the optical dilution outlined in [60–64], stiffening the dynamics of the suspended mirror, although further R&D is required and ongoing to fabricate mechanical resonators with higher quality factors via optical dilution or other methods [65–69]. The thermal noise spectrum in this paper differs from the flat thermal noise spectrum in previous designs [41, 43] since in this case the thermal heat bath fluctuations are fully shaped by the interferometer, except coupled indirectly by the mechanically suspended mirror. Overall it was found that at low frequencies the thermal noise contribution follows the vacuum noise except it is significantly larger by a factor $\gamma_{\text{opt}}/\gamma_m \gg 1$, while the high-frequency thermal noise has a flat contribution.

Another issue is the control of the unstable dynamics of the system. Previously in [41] a stabilizing controller was constructed, however the time delay of the control signal from the arm cavities to the unstable filter were neglected. If they are included, it can be shown that the achievable phase margin will be very small. One other option is to use local sensing control to locally control the unstable filter, eliminating the time delay. Unfortunately, this will impart significant additional noise on the measurement readout, however as Denis Martynov has discovered [70] this local sensing noise can be cancelled out in post-processing by combining the local sensing readout and main readout optimally. An example of a local sensing control scheme for the transmission readout setup is given in Fig. 6.

Finally, for the analysis of future GW detectors we will relax the single-mode approximation, as well as the resolved sideband regime approximation which is manifested in the analysis as the rotating wave approximation, specifically $\gamma_f \ll \omega_m$. This will be performed in a followup paper.

V. ACKNOWLEDGEMENTS

We would like to thank members of the LSC AIC, MQM, and QN groups for fruitful discussions. J.B. is supported by STFC and School of Physics and Astronomy at the University of Birmingham. J.B., P.J., A.F., D.M., and H.M. acknowledge the additional support from the Birmingham Institute for Gravitational Wave Astronomy. H.M. is also supported by UK STFC Ernest Rutherford Fellowship (Grant No. ST/M005844/1).

-
- [1] B. Abbott *et al.*, *Phys. Rev. Lett.* **116**, 241103 (2016).
 - [2] B. Abbott *et al.*, *Phys. Rev. Lett.* **119**, 141101 (2017).
 - [3] B. Abbott *et al.*, *Phys. Rev. Lett.* **119**, 161101 (2017).
 - [4] B. Abbott *et al.*, *ArXiv e-prints* (2018).
 - [5] J. Read, C. Markakis, M. Shibata, K. Uryu, J. Creighton, and J. Friedman, *Phys. Rev. D* (2009).
 - [6] A. Bauswein and H.-T. Janka, *Phys. Rev. Lett.* **108** (2012).
 - [7] J. Aasi *et al.*, *Class. Quantum Grav.* **32**, 074001 (2015).
 - [8] F. Acernese *et al.*, *Class. Quantum Grav.* **32**, 024001 (2015).
 - [9] B. P. Abbott *et al.*, *Class. Quantum Grav.* **34**, 044001 (2017).
 - [10] M. Punturo *et al.*, *Class. Quantum Grav.* **27**, 194002 (2010).
 - [11] J. Mizuno, *Comparison of optical configurations for laser-interferometric gravitational-wave detectors*, Ph.D. thesis, University of Hannover (1995).
 - [12] V. B. Braginsky, M. L. Gorodetsky, F. Y. Khalili, and K. S. Thorne, in *American Inst. of Phys. Conference Series*, Vol. 523, edited by S. Meshkov (2000) pp. 180–190.
 - [13] M. Tsang, H. M. Wiseman, and C. M. Caves, *Phys. Rev. Lett.* **106** (2011).
 - [14] H. Miao, R. X. Adhikari, Y. Ma, B. Pang, and Y. Chen, *Phys. Rev. Lett.* **119** (2017).
 - [15] C. Caves, *Phys. Rev. D* **23**, 1693 (1981).
 - [16] H. J. Kimble, Y. Levin, A. B. Matsko, K. S. Thorne, and S. P. Vyatchanin, *Phys. Rev. D* **65**, 022002 (2001).
 - [17] K. McKenzie, N. Grosse, W. P. Bowen, S. E. Whitcomb, M. B. Gray, D. E. McClelland, and P. K. Lam, *Phys. Rev. Lett.* **93**, 161105 (2004).
 - [18] E. Oelker, T. Isogai, J. Miller, M. Tse, L. Barsotti, N. Mavalvala, and M. Evans, *Phys. Rev. Lett.* **116**, 041102 (2016).
 - [19] R. Schnabel, *Phys. Rep.* **684**, 1 (2017).
 - [20] M. J. Yap, J. Cripe, G. L. Mansell, *et al.*, *ArXiv e-prints* (2018).
 - [21] N. Aggarwal, T. Cullen, J. Cripe, *et al.*, *ArXiv e-prints* (2018).
 - [22] H. Rehbein, J. Harms, R. Schnabel, and K. Danzmann, *Phys. Rev. Lett.* **95** (2005).
 - [23] V. Peano, H. G. L. Schwefel, C. Marquardt, and F. Marquardt, *Phys. Rev. Lett.* **115** (2015).
 - [24] M. Korobko, L. Kleybolte, S. Ast, H. Miao, Y. Chen, and R. Schnabel, *Phys. Rev. Lett.* **118** (2017).
 - [25] M. Korobko, Y. Ma, Y. Chen, and R. Schnabel, “Quantum boost for gravitational-wave observatories,” (2019), in preparation; LIGO DCC P1900024-v1.
 - [26] M. Evans, L. Barsotti, P. Kwee, J. Harms, and H. Miao, *Phys. Rev. D* **88**, 022002 (2013).
 - [27] H. Miao, H. Yang, R. X. Adhikari, and Y. Chen, *Class. Quantum Grav.* **31**, 165010 (2014).
 - [28] J. Miller, L. Barsotti, S. Vitale, P. Fritschel, M. Evans, and D. Sigg, *Phys. Rev. D* **91** (2015).
 - [29] S. Hild *et al.*, *Class. Quantum Grav.* **28**, 094013 (2011).

- [30] The LIGO Scientific Collaboration, *Nat. Phys.* **7**, 962 (2011), [arXiv:1109.2295 \[quant-ph\]](#).
- [31] The LIGO Scientific Collaboration, *Nat. Phot.* **7**, 613 (2013).
- [32] H. Grote, K. Danzmann, K. L. Dooley, R. Schnabel, J. Slutsky, and H. Vahlbruch, *Phys. Rev. Lett.* **110** (2013).
- [33] A. Wicht, K. Danzmann, M. Fleischhauer, M. Scully, G. Müller, and R.-H. Rinkleff, *Optics Comm.* **134**, 431 (1997).
- [34] A. Wicht, M. Müller, R.-H. Rinkleff, A. Rocco, and K. Danzmann, *Optics Comm.* **179**, 107 (2000).
- [35] S. Wise, G. Mueller, D. Reitze, D. Tanner, and B. Whiting, *Class. Quantum Grav.* **21** (2004).
- [36] D. Blair, L. Ju, C. Zhao, *et al.*, *Science China Phys., Mech. & Astro.* **58** (2015).
- [37] G. S. Pati, M. Salit, K. Salit, and M. S. Shahriar, *Phys. Rev. Lett.* **99** (2007).
- [38] H. Yum and J. Scheuer, *Journal of Lightwave Tech.* **31** (2013).
- [39] M. Zhou, Z. Zhou, and S. M. Shahriar, *Phys. Rev. D* **92** (2015).
- [40] Y. Ma, H. Miao, C. Zhao, and Y. Chen, *Phys. Rev. A* **92** (2015).
- [41] H. Miao, Y. Ma, C. Zhao, and Y. Chen, *Phys. Rev. Lett.* **115**, 211104 (2015).
- [42] M. Zhou and S. M. Shahriar, *Phys. Rev. D* **98** (2018).
- [43] H. Miao, H. Yang, and D. Martynov, *Phys. Rev. D* (2017).
- [44] R. Boyd, *Nonlinear Optics*, 3rd ed. (Elsevier Science, 2003).
- [45] A. Thüring, H. Lück, and K. Danzmann, *Phys. Rev. E* **72** (2005).
- [46] A. Thüring, R. Schnabel, H. Lück, and K. Danzmann, *Opt. Lett.* **32**, 985 (2007).
- [47] Y. Chen, *Journal of Phys. B: Atomic, Molecular and Opt. Phys.* **46**, 104001 (2013).
- [48] M. Aspelmeyer, T. J. Kippenberg, and F. Marquardt, *Rev. Mod. Phys.* **86**, 1391 (2014).
- [49] C. K. Law, *Phys. Rev. A* **51**, 2537 (1995).
- [50] C. M. Caves and B. L. Schumaker, *Phys. Rev. A* **31**, 3068 (1985).
- [51] K. J. Blow, R. Loudon, S. J. D. Phoenix, and T. J. Shepherd, *Phys. Rev. A* **42**, 4102 (1990).
- [52] The method in [47] reproduces the quantum Langevin equation of [53] and [54, p. 158], and also [48, 58], in which the setup is known as input-output theory of open quantum systems [48]. Note that a simple cavity coupled to an external bosonic field is mechanically equivalent to a mechanical mass coupled to an external heat bath, as evident by comparing equations 8 and 9.
- [53] C. W. Gardiner and M. J. Collett, *Phys. Rev. A* **31**, 3761 (1985).
- [54] C. Gardiner and P. Zoller, *Quantum Noise* (Springer Berlin Heidelberg, 2010).
- [55] A. Buonanno and Y. Chen, *Phys. Rev. D* **65**, 042001 (2002).
- [56] A. Buonanno and Y. Chen, *Phys. Rev. D* **67**, 062002 (2003).
- [57] V. Braginsky and F. Khalilli, *Quantum Measurements* (Cambridge University Press, 1992).
- [58] A. A. Clerk, M. H. Devoret, S. M. Girvin, F. Marquardt, and R. J. Schoelkopf, *Rev. of Modern Phys.* **82**, 1155 (2010).
- [59] H. Miao, *Exploring Macroscopic Quantum Mechanics in Optomechanical Devices*, Ph.D. thesis, The university of western Australia (2010).
- [60] T. Corbitt, Y. Chen, E. Innerhofer, H. Müller-Ebhardt, D. Ottaway, H. Rehbein, D. Sigg, S. Whitcomb, C. Wipf, and N. Mavalvala, *Phys. Rev. Lett.* **98**, 150802 (2007).
- [61] D. E. Chang, K.-K. Ni, O. Painter, and H. J. Kimble, *New Journal of Phys.* **14**, 045002 (2012).
- [62] K.-K. Ni, R. Norte, D. J. Wilson, J. D. Hood, D. E. Chang, O. Painter, and H. J. Kimble, *Phys. Rev. Lett.* **108** (2012).
- [63] W. Z. Korth, H. Miao, T. Corbitt, G. D. Cole, Y. Chen, and R. X. Adhikari, *Phys. Rev. A* **88** (2013).
- [64] C. Reinhardt, T. Müller, A. Bourassa, and J. C. Sankey, *Phys. Rev. X* **6** (2016).
- [65] D. Chen, A. Kovach, X. Shen, S. Poust, and A. M. Armani, *ACS Photonics* **4**, 2376 (2017).
- [66] Y. Tsaturyan, A. Barg, E. S. Polzik, and A. Schliesser, *Nature Nanotechnology* **12**, 776 (2017).
- [67] M. Rossi, D. Mason, J. Chen, Y. Tsaturyan, and A. Schliesser, *Nature* **563**, 53 (2018).
- [68] M. Page, J. Fontaine, X. Chen, C. Zhao, L. Ju, D. Blair, H. Pan, and S. Chao, *Phys. Lett. A* (2017).
- [69] M. Page, J. Qin, J. L. Fontaine, C. Zhao, L. Ju, and D. Blair, *Phys. Rev. D* **97** (2018).
- [70] D. Martynov, “Local sensing control scheme for unstable filter,” (2019), in preparation.